



Review

Current Perspectives on ^{89}Zr -PET Imaging

Joon-Kee Yoon ^{1,*}, Bok-Nam Park ¹, Eun-Kyoung Ryu ², Young-Sil An ¹ and Su-Jin Lee ¹

¹ Department of Nuclear Medicine & Molecular Imaging, Ajou University School of Medicine, Worldcup-ro 164, Suwon 16499, Korea; curies@hanmail.net (B.-N.P.); aysays77@naver.com (Y.-S.A.); suesj@naver.com (S.-J.L.)

² Division of Magnetic Resonance, Korea Basic Science Institute, 162, Yeongudanji-ro, Cheongju 28119, Korea; ekryu@kbsi.re.kr

* Correspondence: jkyoon3@ajou.ac.kr; Tel.: +82-31-219-4303

Received: 22 May 2020; Accepted: 15 June 2020; Published: 17 June 2020



Abstract: ^{89}Zr is an emerging radionuclide that plays an essential role in immuno-positron emission tomography (PET) imaging. The long half-life of ^{89}Zr ($t_{1/2} = 3.3$ days) is favorable for evaluating the in vivo distribution of monoclonal antibodies. Thus, the use of ^{89}Zr is promising for monitoring antibody-based cancer therapies. Immuno-PET combines the sensitivity of PET with the specificity of antibodies. A number of studies have been conducted to investigate the feasibility of ^{89}Zr immuno-PET imaging for predicting the efficacy of radioimmunotherapy and antibody therapies, imaging target expression, detecting target-expressing tumors, and the monitoring of anti-cancer chemotherapies. In this review, we summarize the current status of PET imaging using ^{89}Zr in both preclinical and clinical studies by highlighting the use of immuno-PET for the targets of high clinical relevance. We also present ^{89}Zr -PET applications other than immuno-PET, such as nanoparticle imaging and cell tracking. Finally, we discuss the limitations and the ongoing research being performed to overcome the remaining hurdles.

Keywords: positron emission tomography; ^{89}Zr ; monoclonal antibody; oncological imaging

1. Introduction

Positron emission tomography (PET) is a widely used imaging technology in clinical oncology. Among the radiotracers used for PET imaging, ^{18}F -fluorodeoxyglucose (FDG) has played a remarkable role in staging, restaging, detecting recurrences, and predicting the prognosis of various cancers [1]. Although ^{18}F -FDG is still a key radiotracer, recently, radiopharmaceuticals other than ^{18}F -FDG have been thoroughly investigated to predict and monitor therapeutic responses along with the development of targeted therapies [2]. Radioisotopes with short half-lives, such as ^{18}F ($t_{1/2} = 110$ min), ^{11}C ($t_{1/2} = 20$ min) and ^{13}N ($t_{1/2} = 10$ min), which are common in clinical practice, have the advantage of low radiation exposure. However, they are not optimal for long circulating probes, such as the monoclonal antibody (mAb). Therefore, radiolabeling with long-lived radioisotopes such as ^{124}I ($t_{1/2} = 4.2$ days), ^{64}Cu ($t_{1/2} = 12.7$ h), and ^{89}Zr ($t_{1/2} = 3.3$ days) is required for the better assessment of the biodistribution of such tracers [3,4].

^{89}Zr is a positron-emitting radionuclide that can be produced by a medical cyclotron. The first production of ^{89}Zr for the labeling of mAb was performed in 1986 by proton bombardment using a solid target, $^{89}\text{Y}(p,n)^{89}\text{Zr}$ [5]. ^{89}Zr decays in two ways (positron emission, 23% and electron capture, 77%) by emitting two important γ -rays: 909 KeV photons during the deactivation of $^{89\text{m}}\text{Y}$ and 511 KeV photons from the positron–electron annihilation (Figure 1A). These photons can be separated by setting the energy windows of PET. In addition, they do not coincide because of the long half-life of $^{89\text{m}}\text{Y}$. ^{89}Zr has a relatively short positron range by emitting low energy β^+ rays ($E_{\beta^+, \text{ave}} = 396$ KeV), which facilitates high-resolution PET imaging.

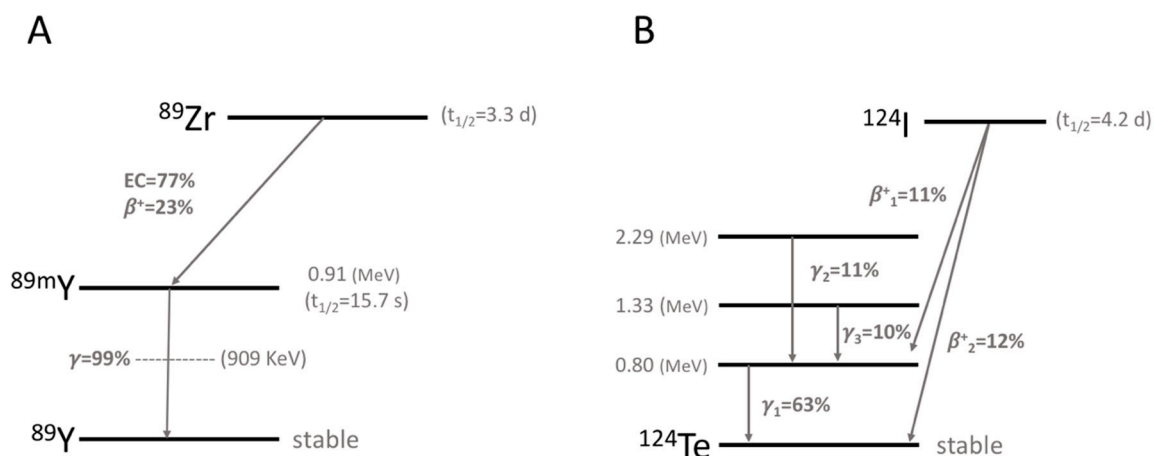


Figure 1. Radioactive decay scheme for ^{89}Zr (A) and ^{124}I (B).

When ^{89}Zr is used for immuno-PET imaging, it has a few advantages over another long-life positron emitter, ^{124}I . As the positron range of ^{89}Zr is shorter than that of ^{124}I due to its lower positron energy ($E_{\beta^+, \text{ave}}$ for $^{124}\text{I} = 819$ KeV, Figure 1B), ^{89}Zr -PET has a superior spatial resolution to ^{124}I -PET [6,7]. ^{124}I does not residualize (trapped within the cells after catabolism of the radiolabeled mAbs) and is rapidly released from the cells when it is labeled to mAbs. Meanwhile, ^{89}Zr internalizes and residualizes after binding to the surface of cells. This difference results in 1.5- to 3-fold higher tumor uptake for ^{89}Zr -labeled mAb than for ^{124}I -labeled mAb [7,8]. Some disadvantages of ^{124}I are its high cost, high impurity, and long production time. ^{89}Zr can be produced at a low cost within a few hours and is easy to purify because fewer contaminants must be removed.

As ^{89}Zr is a metallo-radionuclide, it is stably bound as long as its bifunctional chelator is conjugated to its probes. Since it was first evaluated in 1992, desferrioxamine B (DFO) has been the most popular chelator for ^{89}Zr labeling (Figure 2) [9]. DFO originated from the iron-binding siderophores and consists of hydroxamate groups as the binding site for ^{89}Zr [10]. With the successful labeling of ^{89}Zr to mAbs using DFO, various ^{89}Zr -chelating ligands have been developed [11].

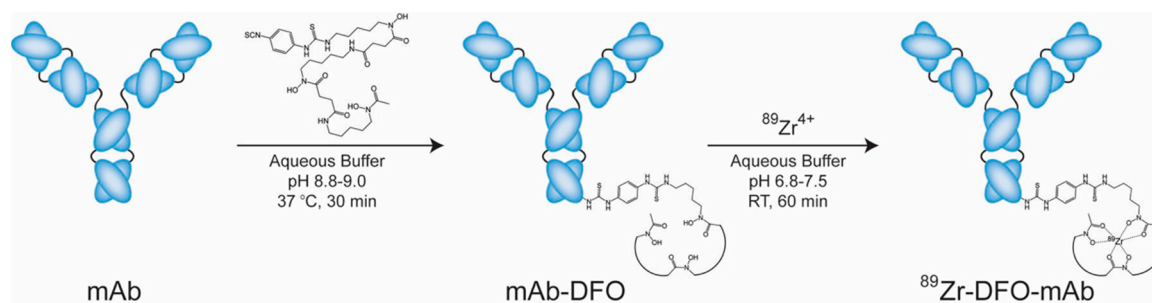


Figure 2. Scheme of the bioconjugation and radiolabeling of ^{89}Zr -desferrioxamine B (DFO)-J591. This is adapted from Zeglis, B. M., Lewis, J. S. The bioconjugation and radiosynthesis of ^{89}Zr -DFO-labeled antibodies. *J. Vis. Exp.* **2015**, 96, e52521, doi:10.3791/52521.

2. ^{89}Zr -PET Imaging in the Literature

With the success of synthesizing ^{89}Zr -labeled antibodies, the number of preclinical and clinical studies related to ^{89}Zr -PET imaging has markedly grown over the last three decades. As of early 2019, more than 300 original articles on the production, radiolabeling chemistry, and preclinical and clinical studies of ^{89}Zr have been published according to a search of Pubmed. When classified by the tracers labeled, antibodies (whole or fragments) and antibody mimetics, occupy more than 70% of those studies, followed by nanoparticles (NPs), proteins, peptides, and cells. For the last 10 years, the number of antibodies and antibody fragments approved by the Food and Drug Administration (FDA) has greatly

increased from 22 (2010) to 93 (2018). Among these, 17 antibodies were labeled to ^{89}Zr and evaluated as PET imaging agents (Table 1). Trastuzumab [12–16] is the most frequently studied antibody, followed by bevacizumab [17–21], cetuximab [22–24], and rituximab [25,26]. Consequently, human epidermal growth factor receptor-2 (HER2), epidermal growth factor receptor (EGFR), vascular endothelial growth factor-A (VEGF-A), cluster of differentiation (CD) 20, and prostate specific membrane antigen (PSMA) are the most frequently explored targets. Researchers have also evaluated several investigational drugs, such as imgatuzumab [27]. Several clinical studies have already been published, but preclinical studies are still much more common than in clinical studies.

Table 1. FDA-approved mAbs used for ^{89}Zr -PET

| Name | Trade Name | Type | Target |
|----------------------|--------------------|-----------|-----------------------|
| Atezolizumab | Tecentriq | humanized | PD-L1 |
| Bevacizumab | Avastin | humanized | VEGF-A |
| Brentuximab vedotin | Adcentris | chimeric | CD30 |
| Cetuximab | Erbitux | chimeric | EGFR |
| Daratumumab | Darzalex | human | CD38 |
| Girentuximab | Rencarex | chimeric | Carbonic anhydrase-IX |
| Ibritumomab tiuxetan | Zevalin | mouse | CD20 |
| Nimotuzumab | Theracim, Theraloc | humanized | EGFR |
| Nivolumab | Opdivo | human | PD-1 |
| Obinutuzumab | Gazyva | humanized | CD20 |
| Ofatumumab | Arzerra | human | CD20 |
| Panitumumab | Vectibix | human | EGFR |
| Pembrolizumab | Keytruda | humanized | PD-1 |
| Pertuzumab | Omnitarg | humanized | HER2 |
| Rituximab | MabThera, Rituxan | chimeric | CD20 |
| Tositumomab | Bexxar | mouse | CD20 |
| Trastuzumab | Herceptin | humanized | HER2 |

The first small animal PET images using ^{89}Zr were reported in 1997 [28]. ^{89}Zr was labeled to mAb 323/A3, which was derived by immunizing mice with human breast cancer cells. PET images were acquired with a clinical PET camera 55 h after intravenous injection and showed specific tumor uptake in mice bearing ovarian cancer xenografts. The first human study was published in 2006 [29]. In patients with squamous head and neck cancers, PET imaging with ^{89}Zr -labeled chimeric mAb U36 localized cervical lymph node metastasis with a high accuracy (93%). ^{89}Zr immuno-PET images were obtainable for up to 144 h after injection.

The term ‘immuno-PET’ first appeared in the literature in 1999 [30]. By combining the sensitivity of PET imaging and the specificity of antibodies, immuno-PET imaging has become a promising tool for monitoring the heterogeneity of specific gene expression and predicting the efficacy of targeted therapies. From a technical perspective, immuno-PET is basically an extension of two nuclear medicine modalities, radioimmunosintigraphy and radioimmunotherapy. Immuno-PET images have a better resolution than the radioimmunosintigraphies obtained by gamma cameras; in addition, immuno-PET images can be used as a surrogate marker for radioimmunotherapy.

In this review, we summarize the current status of ^{89}Zr -PET imaging by highlighting the application of immuno-PET for the targets of high clinical relevance. For every topic, oncological applications will primarily be addressed. We also introduce ^{89}Zr -PET imaging other than immuno-PET, such as nanoparticle imaging. Finally, the limitations and current studies to overcome the hurdles are discussed.

3. Preclinical and Human Studies in ^{89}Zr Immuno-PET Imaging

3.1. Immuno-PET Targeting HER2

HER2 belongs to a member of the ErbB family receptor tyrosine kinases: EFGR, HER2, HER3, and HER4. HER2 plays a critical role in the angiogenesis, differentiation, metastasis, proliferation,

and survival of cancer cells. The increased expression of HER2 is found in a number of cancers, including breast cancer, colon cancer, lung cancer, ovarian cancer, and stomach cancer [31]. Trastuzumab is one of the most effective therapeutic mAbs and also occupies the majority of HER2-targeting immuno-PET studies. On the other hand, only a few studies explored the feasibility of ^{89}Zr -pertuzumab PET imaging [32,33].

Gamma camera imaging with ^{111}In ($t_{1/2} = 2.8$ days) was used for years as a surrogate marker for the optimal distribution of therapeutic mAbs [34,35]. ^{89}Zr -trastuzumab is specific for HER2 positive tumors and shows a similar biodistribution to ^{111}In -trastuzumab when injected into mice bearing HER2-positive tumors [12]. The only difference is a slight increase in the bone marrow uptake for ^{89}Zr -trastuzumab, which was probably due to the accumulation of free ^{89}Zr . Considering the advantage of more accurately quantifying the tracer uptake and dose calculation of PET, ^{89}Zr -trastuzumab PET imaging could be a better option for monitoring therapeutic mAbs.

The optimal time interval between the intravenous injection of ^{89}Zr -trastuzumab and PET imaging for a high tumor to background contrast is 4–8 days [13,16,33,36]. If only an imaging study is performed, the optimal dose for ^{89}Zr -trastuzumab is 50 mg. Meanwhile, the optimal dose reduces to 10 mg during trastuzumab therapy because the hepatic clearance of ^{89}Zr -trastuzumab is slow due to the high blood concentration of trastuzumab and thus a smaller dose can be used to achieve good tumor uptake [16]. ^{89}Zr -trastuzumab can detect most metastatic sites (liver and bone) in patients with HER2-positive breast cancer [16]. On the other hand, it was shown to detect unsuspected HER2-positive metastatic sites even in patients with HER2-negative primary breast cancer, indicating the heterogeneity of the tumors [14,37]. Evaluating the HER2 status of tumors is crucial for clinical decision making for patients planning anti-HER2 therapy. A whole body evaluation of HER2 expression with ^{89}Zr -trastuzumab PET is helpful, particularly when a tumor biopsy is unfeasible. The imaging results for HER2 expression may support or change the treatment plans [38,39].

The responses to anti-HER2 therapy other than mAbs can be monitored by ^{89}Zr -trastuzumab PET. The heat shock protein 90 inhibitor-induced early downregulation and the late recovery of HER2 expression was shown via a ^{89}Zr -trastuzumab PET in xenograft models [40,41]. The ^{89}Zr -trastuzumab PET also displayed a tyrosine kinase inhibitor (afatinib and lapatinib)-induced reduction in HER2 expression [15,42]. The heterogeneous uptake of ^{89}Zr -trastuzumab under PET reflects the genomic heterogeneity of tumors, which is related to the mixed response to afatinib treatment [43].

Based on a few human studies, the estimated radiation dose of ^{89}Zr -trastuzumab PET for patients is about 0.54 mSv/MBq [13,16]. Considering the usual dose (37–74 MBq) for ^{89}Zr -trastuzumab PET, this value is 2–4 times higher than that of ^{18}F -FDG PET. This is one of the major pitfalls to overcome before adopting ^{89}Zr -PET for clinical use.

Similar to ^{89}Zr -trastuzumab, the optimal time for ^{89}Zr -pertuzumab PET is 5–8 days after injection. ^{89}Zr -pertuzumab was able to detect HER2-positive brain metastasis in a patient with heterogeneous HER2 expression for primary tumors, indicating the usefulness of immuno-PET imaging for predicting the response to targeted therapy [33]. ^{89}Zr -pertuzumab was safe; however, the effective dose was as high as that of ^{89}Zr -trastuzumab (0.54 mSv/MBq).

Next-generation antibodies include antibody–drug conjugates (ADCs), immune checkpoint inhibitors, mAbs fused with biological toxins or cytokines, and fragmented antibodies. Immuno-PET could be helpful in the development of ADCs by identifying the presence of a certain biomarker and predicting the therapeutic response (“companion diagnostics”) [44]. Trastuzumab emtansine (T-DM1) is a good example of an ADC that covalently links a cytotoxic agent, DM1, to mAb. For progressive triple-negative breast cancers, baseline ^{89}Zr -trastuzumab PET was able to predict the treatment failure of T-DM1. The early response evaluated by PET after 1 cycle of T-DM1 treatment correlated well with the prognosis [45].

3.2. Immuno-PET Targeting EGFR

EGFR, also known as HER1, is also a member of the ErbB family receptor tyrosine kinase, and its overexpression of EGFR can be observed in breast cancer, head-and-neck cancer, non-small cell lung cancer, renal cancer, ovarian cancer, and colon cancer. EGFR is involved in the differentiation, proliferation, and survival of various cancer cells and is thus related to a poor prognosis, shorter survival, aggressive growth, and invasiveness of cancers [46].

^{177}Lu ($t_{1/2} = 6.7$ days; β , 0.497 MeV) is a β^- -emitting radionuclide, which is promising for cancer therapy when it is labeled to antibodies or peptides [40,47]. To improve therapeutic efficacy, it is essential to predict its in vivo distribution. ^{89}Zr -cetuximab and ^{177}Lu -cetuximab show similar biodistribution over organs, except for a higher bone marrow uptake for ^{89}Zr -cetuximab at 48, 72 and 144 h after injection [48]. With careful consideration of the bone marrow uptake, ^{89}Zr -PET may be useful for selecting candidates for radioimmunotherapy or radionuclide peptide therapy.

EGFR-expressing malignant tumors that are refractory under conventional chemotherapy and radiotherapy may benefit from targeted therapy with cetuximab. However, the tumoral heterogeneity of EGFR expression in some patients hinders successful treatment by cetuximab. PET imaging with ^{89}Zr -cetuximab presented a difference in the EGFR expression in patients with head-and-neck cancers and in those with advanced colorectal cancers, as revealed by the standardized uptake value (SUV) [22,23]. For colorectal cancers, the tumor uptake of ^{89}Zr -cetuximab correlated well with the therapeutic outcome with cetuximab [23]. The uptake of ^{89}Zr -nimotuzumab and ^{89}Zr -panitumumab was also specific and correlated well with the EGFR expression of tumors in colorectal and breast cancer models [49,50].

The whole-body effective dose of ^{89}Zr -cetuximab PET (0.61 mSv/MBq) was similar to that of ^{89}Zr -trastuzumab (0.54 mSv/MBq). The liver has the highest absorbed dose (2.60 mGy/MBq), which is 0.51 mGy/MBq for red marrow [24]. On the other hand, ^{89}Zr -panitumumab has a much lower whole-body effective dose at 0.26 mSv/MBq. Additionally, PET images are obtainable after 5–7 days by injecting as little as 37 MBq of ^{89}Zr -panitumumab [51]. Considering the radiation exposure, ^{89}Zr -panitumumab is a safer radiopharmaceutical than ^{89}Zr -cetuximab.

Various fragmented antibodies and antibody mimetics have been developed to overcome the shortcomings of whole antibodies. Affibody is an engineered protein that consists of 59 amino acid (~6 kDa). Rapid tumor penetration and blood clearance are advantages of the affibody. The ^{89}Zr -labeled EGFR-specific affibody, ZEGFR:03115, showed tumor uptake as early as 3 h after injection. There was a good correlation between the tumor uptake of the ^{89}Zr -affibody and EGFR expression [52]. These findings demonstrate that ^{89}Zr -immuno PET imaging can be a good predictor for targeted antibody therapy.

3.3. Immuno-PET Targeting VEGF-A

VEGF-A binds to VEGF receptors 1 and 2 and then acts as a proangiogenic factor in normal tissues and tumors. VEGF is involved in endothelial cell proliferation, survival, migration, and vascular permeability. The overexpression of VEGF is observed in many types of cancers [53].

Bevacizumab binds to all isoforms of VEGF-A and is the only FDA-approved mAb used for immuno-PET imaging. ^{89}Zr -bevacizumab PET has a high sensitivity (96%) for detecting VEGF expressing primary breast cancers and high specificity (100%) for lymph node metastasis [21]. The ^{89}Zr -bevacizumab uptake given by the maximum SUV is correlated with the VEGF-A concentration and proliferation index of the primary tumors.

Unlike ^{18}F -FDG PET, ^{89}Zr -bevacizumab PET shows a very low brain uptake, enabling the visualization of VEGF-A expressing tumors in the brain and adjacent organs [18,54]. The von Hippel–Lindau (VHL) syndrome is a rare genetic disorder characterized by a variety of tumors including hemangioblastomas, retinal angiomas, and visceral cysts. Locally produced VEGF-A mediates angiogenesis during disease manifestation; whole-body surveillance for VEGF expressing tumors is required for anti-angiogenesis therapy with bevacizumab [18]. Diffuse pontine glioma

is a rare brainstem tumor that is refractory to systemic chemotherapies. VEGF is overexpressed in diffuse pontine glioma. Thus, bevacizumab therapy can be effective in an individual patient [54]. Immuno-PET using ^{89}Zr -bevacizumab may be helpful in identifying potential responders to treatment among these patients.

^{89}Zr -bevacizumab PET can be used for monitoring anti-angiogenesis treatment. ^{89}Zr -bevacizumab uptake, VEGF-A concentration, and microvessel density in ovarian cancer xenografts decreased through the treatment of a mammalian target of the rapamycin inhibitor, everolimus [55]. In patients with metastatic renal cell carcinoma, the change in the maximum SUV between 2 and 6 weeks was an indicator for the response of the everolimus treatment. PET-guided treatment led to stable disease for all patients [56]. The therapeutic response to bevacizumab/interferon- α can be assessed by interim ^{89}Zr -bevacizumab PET. Only half of the lesions had a ^{89}Zr -bevacizumab uptake because of the heterogeneous expression of VEGF [20]. Sunitinib, a multi-targeted tyrosine kinase inhibitor, exerts an anti-angiogenic effect by inhibiting VEGF receptors 1 and 2 [57]. Immuno-PET visualized the rebound growth of cancers via the discontinuation of sunitinib [20,58]. The ^{89}Zr -bevacizumab uptake in metastatic renal cell carcinomas decreased by 14.3% after 2 weeks of therapy but increased by 72.6% at 2 weeks after discontinuation [20]. ^{89}Zr -ranibizumab PET also visualized the rebound of ovarian cancer xenografts after the discontinuation of sunitinib treatment [58].

Apart from oncologic diseases, ^{89}Zr -bevacizumab PET may be used for detecting vulnerable plaques. VEGF release in atherosclerotic plaques is known to make the plaques vulnerable. The ^{89}Zr -bevacizumab PET detected all the carotid endarterectomy specimens *ex vivo* and correlated with the VEGF expression revealed by immunohistochemical staining [19].

3.4. Immuno-PET Targeting CD20

CD20 is a non-glycosylated phosphoprotein that is expressed on the surface of B-cell hematopoietic malignancies such as B-cell non-Hodgkin lymphoma (NHL) and chronic lymphocytic leukemia [59]. Various CD20-targeting mAbs are applied to treat B-cell-related malignancies and autoimmune diseases. To date, ^{89}Zr -PET imaging with five different mAbs has been applied: ibritumomab, rituximab, tositumomab, obinutuzumab, and ofatumumab.

The first FDA-approved radioimmunotherapy was ^{90}Y -ibritumomab tiuxetan (Zevalin[®], Acrotech Biopharma, LLC, East Windsor, NJ, USA). As ^{90}Y is a pure β -emitting radioisotope, ^{111}In has been used as a surrogate to predict the response to ^{90}Y [60]. ^{89}Zr is a candidate to replace ^{111}In because ^{89}Zr and ^{90}Y ($t_{1/2} = 2.7$ days) have similar physical half-lives. The biodistribution of ^{89}Zr -zevalin was not affected by co-injected ^{90}Y -zevalin, resulting in a similar biodistribution between ^{89}Zr -zevalin and ^{90}Y -zevalin, except for liver and bone marrow [61,62]. ^{89}Zr -zevalin showed a significantly higher uptake in the liver, thigh bone and sternum at 72 and 144 h after injection, as compared to ^{90}Y -zevalin [61]. In patients with NHL, pre-treatment ^{89}Zr -zevalin PET imaging can be used to determine the dose-limiting organs in ^{90}Y -zevalin treatment [62].

^{89}Zr -rituximab PET is useful for detecting CD20 expression in patients with diffuse large B-cell lymphoma. The tumor uptake of ^{89}Zr -rituximab showed a high concordance with CD20 expression when studied with immunohistochemistry [25]. ^{89}Zr -rituximab PET also helped prevent invasive nerve biopsy while determining an optimal therapy for neurolymphomatosis [63].

Besides hematologic malignancies, patients with rheumatoid arthritis may benefit from ^{89}Zr -rituximab PET. B cell-depletion therapy with rituximab is based on the role of the B lymphocyte in the pathogenesis of rheumatoid arthritis and appears to be efficient in some patients with refractory disease [64]. The ^{89}Zr -rituximab uptake of hand joints in PET was significantly higher in the rituximab-responder group. This uptake correlated inversely with the B-cell count in the lymph nodes after treatment [26]. A ^{89}Zr -rituximab PET may thus be helpful in selecting patients who will be responsive to rituximab therapy.

3.5. Immuno-PET Targeting PSMA

PSMA is a transmembrane protein that is heterogeneously expressed on prostate epithelial cells. PSMA is highly expressed in prostate cancers and correlates with the metastasis and progression of prostate cancer [65]. Two important mAbs, 7E11 and J591, are associated with ^{89}Zr immuno-PET imaging. 7E11 is already used for immunoscintigraphy in the form of ^{111}In -labeled capromab pendetide (ProstaScint[®], Cytogen Corporation, Princeton, NJ, USA). ^{89}Zr -7E11 PET has been infrequently studied because 7E11 binds to the intracellular domain of PSMA [66]. On the other hand, J591 binds to the extracellular domain of PSMA. Thus, most immuno-PET studies are associated with J591 mAb and its minibody (IAB2M).

^{89}Zr -J591 PET is used to detect PSMA-expressing tumors [67–69]. Early studies with ^{89}Zr -J591 PET have shown inconsistent results for the diagnostic performance of primary prostate cancers [67,68]. For prostate cancer without metastasis ($n = 11$), there was no difference in Gleason's score between ^{89}Zr -J591 (+) and ^{89}Zr -J591 (–) tumors [67]. Meanwhile, for those with metastatic prostate cancers ($n = 10$), the sensitivity for detecting primary tumors increased to 100%. A ^{89}Zr -J591 PET is also useful for detecting bone metastasis compared to conventional imaging modalities [68]. A subsequent study with a larger population ($n = 50$) of castration-resistant prostate cancers suggested that ^{89}Zr -J591 PET had a higher sensitivity for bone metastasis than conventional imaging methods, while conventional imaging methods were more sensitive for soft tissue lesions [69]. Based on these results, ^{89}Zr -J591 PET could be used for detecting bone metastasis in advanced prostate cancers.

^{89}Zr -J591 PET guided biopsy has very high accuracy for prostate cancer [70]. Compared to ^{18}F -FDG, the longer half-life of ^{89}Zr can help avoid reinjection for biopsy guidance.

^{89}Zr -labeled IAB2M showed a rapid accumulation in tumors and a fast clearance from the blood within 24 h in a prostate cancer model [71]. The ^{89}Zr -IAB2M uptake of bone and lymph node metastases was discernible in as little as 24 h and lasted up to 120 h in patients with prostate cancer [72]. The ^{89}Zr -IAB2M PET clearly visualized recurrent cerebral glioma and metastatic brain tumors from lung cancer, and the tumor to background contrast of the ^{89}Zr -IAB2M uptake was shown to be higher than that of ^{11}C -methionine PET [73]. The ^{89}Zr -IAB2M uptake correlated with PSMA expression [73].

The calculated effective dose from the ^{89}Zr -J591 PET is 0.38 mSv/MBq (14.1 mSv/mCi) [68]. The radiation dose from 37–74 MBq ^{89}Zr -J591 is slightly higher than that of 370 MBq ^{18}F -FDG. The effective dose from the ^{89}Zr -IAB2M PET is 0.41–0.68 mSv/MBq [72,74]. The radiation exposure to medical staff and family is lower than 1 mSv for the first week [72].

3.6. Immuno-PET Targeting CD44

CD44 is a cell-surface glycoprotein involved in many biological processes. The v6 splice variant of CD44 (CD44v6) is involved in tumorigenesis, tumor cell invasion, and metastasis. CD44v6 is expressed in various cancers, predominantly in squamous cell carcinomas [75].

^{89}Zr -labeled mAbs against CD44v6 may be used for the detection of tumors and the prediction of therapies [29,76,77]. ^{89}Zr -labeled chimeric mAb, U36, showed a similar biodistribution to its ^{90}Y -labeled therapeutic counterpart, which enables it to predict the response of radioimmunotherapy [76]. In head-and-neck cancer patients, the diagnostic performance of ^{89}Zr -U36 was comparable to that of conventional imaging methods (29). The ^{89}Zr -labeled humanized mAb, RG7356, also showed specific tumor uptake in CD44+ tumors. The uptake of ^{89}Zr -RG7356 correlated with CD44 expression [77].

3.7. Immuno-PET Targeting HER3

HER3 is also a member of the ErbB family of receptor tyrosine kinases. Due to the lack of intrinsic kinase activity, HER3 forms active heterodimers with other members of the ErbB family and mediates the proliferation, invasion, and metastasis of cancers and resistance to chemotherapy [78].

HER3 expression on various tumors has also been visualized, and the treatment response by ^{89}Zr -anti-HER3 PET has been predicted. PET using ^{89}Zr -labeled lumretuzumab or GSK2849330

successfully demonstrated specific tumor uptake in patients with HER3-expressing tumors [79,80]. It is known that HER3 upregulation during anti-HER therapy is associated with resistance. The tumor uptake of the ^{89}Zr -labeled anti-HER3 affibody, ZHER3:8698, increased under AUY922 treatment and correlated with the HER3 upregulation in MCF-7 xenografts [81].

3.8. Immuno-PET Using Immune Checkpoint Inhibitors

Recently, immunotherapies using immune-checkpoint inhibitors have drawn clinical attention and have been actively investigated for patients who have tumors that are refractory to conventional chemotherapies. The programmed death ligand 1 (PD-L1) of tumor cells binds to the programmed cell death protein 1 (PD-1) of T-cells, resulting in a suppression of the killing effect of T-cells [82]. Various mAbs have been discovered to act against PD-L1 (atezolizumab, avelumab, and durvalumab) and PD-1 (pembrolizumab, nivolumab, and cemiplimab). Of these, atezolizumab, pembrolizumab, and nivolumab have been developed as potential immuno-PET imaging agents. In an animal model, ^{89}Zr -nivolumab PET demonstrated PD-1 expression in T-cells that were activated by human peripheral blood lymphocyte engraftment [83]. In cancer patients, ^{89}Zr -atezolizumab distributes to tumors and various organs, including normal lymphoid tissues. The ^{89}Zr -atezolizumab uptake correlated with overall survival and progression free survival [84]. However, most studies are currently preclinical; thus, further clinical studies are required to corroborate the usefulness of ^{89}Zr -atezolizumab.

3.9. Immuno-PET Targeting Lymphocyte Markers

Immunotherapies for refractory cancers, by increasing tumoral immune response, have shown durable effects in some patients who are responsive. The detection of T-lymphocyte infiltration into the tumor microenvironment is crucial for the early prediction of treatment efficacy [85]. Whole mAbs or engineered antibodies against CD3, CD4 and CD8 have been explored to monitor T-lymphocytes. The ^{89}Zr -anti-CD3 showed a high tumoral uptake and a low background in mice bearing syngeneic tumors. The tumor-to-blood ratio of ^{89}Zr -anti-CD3 was 11.5-fold higher than that of the isotype control [86]. The tumoral uptake of ^{89}Zr -anti-CD3 showed a good correlation with the response to anti-cytotoxic T-lymphocyte antigen-4 therapy in a murine xenograft model. The tumor volume of the high uptake group was significantly smaller than that of the control or the low uptake group [87]. Moreover, ^{89}Zr -anti-CD3 did not change total T-lymphocyte count, but induced a decrease in the CD4/CD8 ratio [86]. CD4 and CD8 T-lymphocytes can be detected by immuno-PET using ^{89}Zr -labeled cys-diabodies against CD4 and CD8. Serial PET imaging at 2, 4 and 8 weeks after hematopoietic stem cell therapy demonstrated the repopulation of T-lymphocytes in lymph nodes and spleen [88]. PET imaging using a recently developed bispecific antibody targeting both T-lymphocytes and tumor cells also allows to detect tumor-infiltrating lymphocytes [89].

4. ^{89}Zr -PET Imaging Other than Immuno-PET

4.1. ^{89}Zr -Labeled Nanoparticles PET

Various radionuclides including ^{198}Au , ^{111}In , ^{64}Cu , $^{125\text{m}}\text{Te}$, ^{188}Re , ^{166}Ho , and $^{99\text{m}}\text{Tc}$ have been used for nanoparticle-based nuclear medicine imaging and therapy [90]. Dozens of studies concerning ^{89}Zr -labeled NPs have already been reported, although only a few are clinical. Researchers suggest that ^{89}Zr -labeled NPs (liposomal NPs, nanocolloids, mesoporous silica NPs, dextran NPs, chitosan NPs, etc.) are also promising for tumor detection, the development of nanoparticle drugs, the monitoring of drug delivery, inflammation imaging, and tumor-associated macrophage (TAM) imaging.

TAMs lead to disease progression in cancer cells by modulating the tumor microenvironment and are thus potential targets for anti-cancer therapy. To predict the efficacy of anti-TAM therapy, it is crucial to monitor the quantity and distribution of TAMs. ^{89}Zr -labeled natural high-density lipoprotein (HDL) and dextran NPs showed favorable tumor uptake [91,92]. The co-localization of these radiotracers

with a macrophage was revealed by histology and fluorescent imaging [91,92]. These results suggest that ^{89}Zr -labeled NPs can be a good tool for monitoring anti-TAM therapy.

Several studies presented evidence for ^{89}Zr -labeled nanocolloidal albumin as a PET imaging agent for sentinel lymph mapping [93–96]. In patients with early colon cancers or oral cavity cancers, PET detected sentinel lymph nodes with a very high sensitivity [95,96]. Due to the long half-life of ^{89}Zr , sentinel lymph node mapping using ^{89}Zr -NPs has the advantages of accomplishing both PET imaging and intraoperative probe detection via the single injection of a radiotracer, even though surgical procedures are performed on another day.

^{89}Zr -labeled NPs for atherosclerotic plaques are good examples of inflammation imaging. HDL mimetic infusion has been studied for years as a method to reduce cardiovascular risk. One of the reasons for the failure of HDL mimetic infusion is its low target delivery. ^{89}Zr -labeled natural HDLs and HDL mimetics are delivered to atherosclerotic plaques by being trapped in the macrophages [97,98]. The uptake of ^{89}Zr -labeled HDL mimetics, CER-001, was slightly higher in plaques than in non-plaque walls and correlated well with the contrast enhancement by magnetic resonance imaging (98). Recent animal studies revealed that ^{89}Zr -labeled dextran or hyaluronan NPs have the ability to detect atherosclerotic plaques and monitor anti-inflammatory therapy [99,100].

4.2. ^{89}Zr -Induced Cerenkov Luminescence Imaging and Therapy

The Cerenkov effect was characterized by Pavel A. Cerenkov in 1934 as the radiation emitted when charged particles (β^+ , β^- , α) travel through an optically transparent insulating material with a velocity that exceeds the speed of light. Cerenkov luminescence imaging has been exploited in a number of preclinical studies. The β^+ particles emitted by ^{89}Zr also produce Cerenkov luminescence. Using ^{89}Zr -J591 and luminescence imaging, prostate cancers were visualized in animal models [101].

Photodynamic therapy requires external light to activate the photosensitizers for cancer therapy. Cerenkov radiation from ^{89}Zr can be used as a light source for this purpose. ^{89}Zr -labeled mesoporous silica NPs have ^{89}Zr and photosensitizers inside their hollows. In a breast cancer model, the tumor suppression effect was greater for the ^{89}Zr -labeled mesoporous silica NPs than for the NPs only, or for the control [102]. The advantage of ^{89}Zr over conventional approaches is that ^{89}Zr 's long half-life facilitates long-term photodynamic therapy.

4.3. Cell Tracking with ^{89}Zr

Due to its old modality, radiolabeled leukocytes, cell tracking is nothing new for nuclear medicine imaging. Thus, it has already been adopted for various types of cell tracking. Using nuclear medicine imaging to evaluate the early distribution and viability of radiolabeled stem cells is a notable example [103]. With the development of cancer immunotherapy, tracking therapeutic cells is becoming more important for predicting the effectiveness of a therapy. ^{89}Zr has a favorable physical half-life for tracking cells in vivo. Additionally, similar to ^{111}In -oxine, ^{89}Zr -oxine can be labeled to cells directly.

Chimeric antigen receptor (CAR) T-cells are transduced to locate specific targets on the surface of tumors. A few drawbacks of CAR T-cells include their poor tumor-targeting ability and normal tissue toxicity [104]. The prediction of therapeutic efficacy by cell tracking is critical to overcome these shortcomings. Direct labeling with ^{89}Zr -oxine allowed the visualization of CAR T-cell migration to tumors in a glioblastoma model [105]. Labeling with ^{89}Zr -oxine did not affect the viability and function of cells. The fragmented antibody F(ab')_2 for T-cell receptors is another candidate that showed high sensitivity for T-cells in an animal model. Transduced cells as small as 4.7×10^4 were detected via PET imaging, and the tumor uptake quantity was proportional to the number of injected cells [106].

^{89}Zr -desferrioxamine-N-chlorosuccinimide (DBN) is also actively studied as a direct cell labeling method. Unlike ^{89}Zr -oxine, ^{89}Zr -DBN binds covalently to the amine groups of cell surface membrane proteins [107]. Although the labeling efficiency was low to moderate (30~50%), ^{89}Zr -DBN was stably bound to human mesenchymal stem cells (hMSCs) for up to 7 days without deteriorating the cellular viability [107]. PET imaging using ^{89}Zr -hMSC that were delivered to the adventitia of the outflow vein

of arteriovenous fistula allowed to track transplanted hMSCs for 3 weeks [108]. More than 90% of the transplanted cells were detected at the site of delivery on day 4, which was decreased by 20% on day 21 [108]. ^{89}Zr -DBN was also labeled to hepatocytes with a labeling efficiency of 20% [109]. The initial amount of homing cells and the subsequent retention was monitored up to 48 h by PET imaging [109].

5. Discussion and Summary

Immuno-PET using ^{89}Zr has the advantage of a high resolution and high specificity. ^{89}Zr immuno-PET visualizes the expression of a variety of genes and reflects the status of tumor heterogeneity. Therefore, ^{89}Zr immuno-PET is a useful modality to predict and evaluate the response of therapeutic mAbs and that of some targeted therapies.

A few points in previous studies should be carefully considered before clinical use. First, as the production of ^{89}Zr requires a medium-energy cyclotron and a solid target system, the use of ^{89}Zr is currently restricted to a small number of countries and institutes. Recent improvements in the yttrium target design facilitated the production of a clinical amount of ^{89}Zr , which may provide a solution to this shortage in supply [110,111]. Another option for the production of ^{89}Zr is using a liquid target. Irradiating the aqueous solution of yttrium nitrate ($\text{Y}(\text{NO}_3)_3 \cdot 6\text{H}_2\text{O}$) generated a significant amount of ^{89}Zr ($0.27 \pm 0.05 \text{ GBq}/\mu\text{A}$)—enough for clinical use in a single institute [112]. A second-generation solution target was employed to reduce the problems of in-target salt precipitation and unstable target pressure. A new target led to double the production quantity of ^{89}Zr ($\sim 370 \text{ MBq}$ in 2 h), which is sufficient for a small number of patients [113].

Second, as shown in previous studies, a significant amount of ^{89}Zr accumulates in the bone marrow when entered into the circulatory system. As most dechelated forms of ^{89}Zr (^{89}Zr -chloride, ^{89}Zr -citrate, and ^{89}Zr -oxalate) accumulate in the bone marrow, this process is attributed to the instability of ^{89}Zr -DFO chelation [30]. Recent studies in radiochemistry are paving the way toward improving stability by changing the structure of DFO or exploiting new chelators [114–120]. A decrease in bone marrow uptake is good for increasing sensitivity to lesions, as well as decreasing bone marrow toxicity for patients.

Compared to ^{18}F -FDG and conventional computed tomography, patients generally receive higher radiation from ^{89}Zr -labeled mAb PET—approximately 20–40 mSv for 37–74 MBq ^{89}Zr . To reduce the radiation dose, a groundbreaking improvement in PET technology is necessary. Digital PET is a good example of successful dose reduction due to the enhanced sensitivity from using a PET equipped with digital silicon photomultipliers [121]. The high sensitivity of digital PET makes it possible to acquire images either with a shorter scan time or with a lower radiopharmaceutical dose. However, considering the relationship between the dose and resolution for ^{89}Zr -PET, further technical improvements are still required.

Author Contributions: Conceptualization, J.-K.Y. and B.-N.P.; methodology, J.-K.Y., and B.-N.P.; writing—original draft preparation, J.-K.Y.; writing—review and editing, E.-K.R., Y.-S.A., S.-J.L., and J.-K.Y.; funding acquisition, J.-K.Y. All authors have read and agreed to the published version of the manuscript.

Funding: This study was supported by the National Research Foundation of Korea grant funded by the Korea government (No. 2017R1A2B2002692).

Conflicts of Interest: The authors declare no conflict of interest. The funders had no role in the design of the study; in the collection, analyses, or interpretation of data; in the writing of the manuscript, or in the decision to publish the results.

Abbreviations

| | |
|-----|-------------------------------------|
| PET | Positron emission tomography |
| FDG | ^{18}F -fluorodeoxyglucose |
| mAb | Monoclonal antibody |
| DFO | Desferrioxamine B |
| NP | Nanoparticle |

| | |
|--------|--|
| FDA | Food and Drug Administration |
| HER2 | Human epidermal growth factor receptor-2 |
| EGFR | Epidermal growth factor receptor |
| VEGF-A | Vascular endothelial growth factor-A |
| CD | Cluster of differentiation |
| PSMA | Prostate specific membrane antigen |
| PD-L1 | Programmed cell death ligand-1 |
| PD-1 | Programmed cell death protein-1 |
| ADCs | Antibody–drug conjugates |
| T-DM1 | Trastuzumab emtansine |
| SUV | Standardized uptake value |
| CD44v6 | v6 splice variant of CD44 |
| TAM | Tumor-associated macrophages |
| HDL | High-density lipoprotein |
| CAR | Chimeric antigen receptor |
| DBN | Desferrioxamine-N-chlorosuccinimide |
| hMSC | Human mesenchymal stem cells |

References

- Hustinx, R.; Benard, F.; Alavi, A. Whole-body FDG-PET imaging in the management of patients with cancer. *Semin. Nucl. Med.* **2002**, *32*, 35–46. [[CrossRef](#)] [[PubMed](#)]
- Sharma, P.; Kumar, R.; Alavi, A. PET/Computed Tomography Using New Radiopharmaceuticals in Targeted Therapy. *PET Clin.* **2015**, *10*, 495–505. [[CrossRef](#)] [[PubMed](#)]
- Zhou, Y.; Baidoo, K.E.; Brechbiel, M.W. Mapping biological behaviors by application of longer-lived positron emitting radionuclides. *Adv. Drug Deliv. Rev.* **2013**, *65*, 1098–1111. [[CrossRef](#)] [[PubMed](#)]
- Kairemo, K.J. Positron emission tomography of monoclonal antibodies. *Acta Oncol.* **1993**, *32*, 825–830. [[CrossRef](#)] [[PubMed](#)]
- Link, J.M.; Krohn, K.A.; Eary, J.F.; Kishore, R.; Lewellen, T.K.; Johnson, M.W.; Badger, C.C.; Richter, K.Y.; Nelp, W.B. Zr-89 for antibody labeling and positron emission tomography. *J. Label. Compd. Radiopharm.* **1986**, *23*, 1297–1298.
- Dalen, J.; Visser, E.; Laverman, P.; Vogel, W.; Oyen, W.; Cortens, F.; Boerman, O. Effect of the positron range on the spatial resolution of a new generation pre-clinical PETscanner using F-18, Ga-68, Zr-89 and I-124. *J. Nucl. Med.* **2008**, *49*, 404.
- Stillebroer, A.B.; Franssen, G.M.; Mulders, P.F.; Oyen, W.J.; van Dongen, G.A.; Laverman, P.; Oosterwijk, E.; Boerman, O.C. ImmunoPET imaging of renal cell carcinoma with (124)I- and (89)Zr-labeled anti-CAIX monoclonal antibody cG250 in mice. *Cancer Biother. Radiopharm.* **2013**, *28*, 510–515. [[CrossRef](#)]
- Fung, E.K.; Cheal, S.M.; Fareedy, S.B.; Punzalan, B.; Beylertgil, V.; Amir, J.; Chalasani, S.; Weber, W.A.; Spratt, D.E.; Veach, D.R.; et al. Targeting of radiolabeled J591 antibody to PSMA-expressing tumors: Optimization of imaging and therapy based on non-linear compartmental modeling. *EJNMMI Res.* **2016**, *6*, 7. [[CrossRef](#)]
- Zeglis, B.M.; Lewis, J.S. The bioconjugation and radiosynthesis of 89Zr-DFO-labeled antibodies. *J. Vis. Exp.* **2015**, e52521. [[CrossRef](#)]
- Meijs, W.E.; Herscheid, J.D.; Haisma, H.J.; Pinedo, H.M. Evaluation of desferal as a bifunctional chelating agent for labeling antibodies with Zr-89. *Int. J. Rad. Appl. Instrum A* **1992**, *43*, 1443–1447. [[CrossRef](#)]
- Bhatt, N.B.; Pandya, D.N.; Wadas, T.J. Recent Advances in Zirconium-89 Chelator Development. *Molecules* **2018**, *23*, 638. [[CrossRef](#)]
- Dijkers, E.C.; Kosterink, J.G.; Rademaker, A.P.; Perk, L.R.; van Dongen, G.A.; Bart, J.; de Jong, J.R.; de Vries, E.G.; Lub-de Hooge, M.N. Development and characterization of clinical-grade 89Zr-trastuzumab for HER2/neu immunoPET imaging. *J. Nucl. Med.* **2009**, *50*, 974–981. [[CrossRef](#)] [[PubMed](#)]
- Laforte, R.; Lapi, S.E.; Oyama, R.; Bose, R.; Tabchy, A.; Marquez-Nostra, B.V.; Burkemper, J.; Wright, B.D.; Frye, J.; Frye, S.; et al. [(89)Zr]Trastuzumab: Evaluation of Radiation Dosimetry, Safety, and Optimal Imaging Parameters in Women with HER2-Positive Breast Cancer. *Mol. Imaging Biol.* **2016**, *18*, 952–959. [[CrossRef](#)] [[PubMed](#)]

14. Ulaner, G.A.; Hyman, D.M.; Ross, D.S.; Corben, A.; Chandarlapaty, S.; Goldfarb, S.; McArthur, H.; Erinjeri, J.P.; Solomon, S.B.; Kolb, H.; et al. Detection of HER2-Positive Metastases in Patients with HER2-Negative Primary Breast Cancer Using ⁸⁹Zr-Trastuzumab PET/CT. *J. Nucl. Med.* **2016**, *57*, 1523–1528. [[CrossRef](#)]
15. Janjigian, Y.Y.; Viola-Villegas, N.; Holland, J.P.; Divilov, V.; Carlin, S.D.; Gomes-DaGama, E.M.; Chiosis, G.; Carbonetti, G.; de Stanchina, E.; Lewis, J.S. Monitoring afatinib treatment in HER2-positive gastric cancer with ¹⁸F-FDG and ⁸⁹Zr-trastuzumab PET. *J. Nucl. Med.* **2013**, *54*, 936–943. [[CrossRef](#)] [[PubMed](#)]
16. Dijkers, E.C.; Oude Munnink, T.H.; Kosterink, J.G.; Brouwers, A.H.; Jager, P.L.; de Jong, J.R.; van Dongen, G.A.; Schroder, C.P.; Lub-de Hooge, M.N.; de Vries, E.G. Biodistribution of ⁸⁹Zr-trastuzumab and PET imaging of HER2-positive lesions in patients with metastatic breast cancer. *Clin. Pharmacol. Ther.* **2010**, *87*, 586–592. [[CrossRef](#)] [[PubMed](#)]
17. Veldhuijzen van Zanten, S.E.M.; Sewing, A.C.P.; van Lingen, A.; Hoekstra, O.S.; Wesseling, P.; Meel, M.H.; van Vuurden, D.G.; Kaspers, G.J.L.; Hulleman, E.; Bugiani, M. Multiregional Tumor Drug-Uptake Imaging by PET and Microvascular Morphology in End-Stage Diffuse Intrinsic Pontine Glioma. *J. Nucl. Med.* **2018**, *59*, 612–615. [[CrossRef](#)]
18. Oosting, S.F.; van Asselt, S.J.; Brouwers, A.H.; Bongaerts, A.H.; Steinberg, J.D.; de Jong, J.R.; Lub-de Hooge, M.N.; van der Horst-Schrivers, A.N.; Walenkamp, A.M.; Hoving, E.W.; et al. ⁸⁹Zr-Bevacizumab PET Visualizes Disease Manifestations in Patients with von Hippel-Lindau Disease. *J. Nucl. Med.* **2016**, *57*, 1244–1250. [[CrossRef](#)] [[PubMed](#)]
19. Golestani, R.; Zeebregts, C.J.; Terwisscha van Scheltinga, A.G.; Lub-de Hooge, M.N.; van Dam, G.M.; Claudemans, A.W.; Dierckx, R.A.; Tio, R.A.; Suurmeijer, A.J.; Boersma, H.H.; et al. Feasibility of vascular endothelial growth factor imaging in human atherosclerotic plaque using (⁸⁹)Zr-bevacizumab positron emission tomography. *Mol. Imaging* **2013**, *12*, 235–243. [[CrossRef](#)] [[PubMed](#)]
20. Oosting, S.F.; Brouwers, A.H.; van Es, S.C.; Nagengast, W.B.; Oude Munnink, T.H.; Lub-de Hooge, M.N.; Hollema, H.; de Jong, J.R.; de Jong, I.J.; de Haas, S.; et al. ⁸⁹Zr-bevacizumab PET visualizes heterogeneous tracer accumulation in tumor lesions of renal cell carcinoma patients and differential effects of antiangiogenic treatment. *J. Nucl. Med.* **2015**, *56*, 63–69. [[CrossRef](#)] [[PubMed](#)]
21. Gaykema, S.B.; Brouwers, A.H.; Lub-de Hooge, M.N.; Pleijhuis, R.G.; Timmer-Bosscha, H.; Pot, L.; van Dam, G.M.; van der Meulen, S.B.; de Jong, J.R.; Bart, J.; et al. ⁸⁹Zr-bevacizumab PET imaging in primary breast cancer. *J. Nucl. Med.* **2013**, *54*, 1014–1018. [[CrossRef](#)] [[PubMed](#)]
22. Even, A.J.; Hamming-Vrieze, O.; van Elmpst, W.; Winnepenninckx, V.J.; Heukelom, J.; Tesselaar, M.E.; Vogel, W.V.; Hoeben, A.; Zegers, C.M.; Vugts, D.J.; et al. Quantitative assessment of Zirconium-89 labeled cetuximab using PET/CT imaging in patients with advanced head and neck cancer: A theragnostic approach. *Oncotarget* **2017**, *8*, 3870–3880. [[CrossRef](#)] [[PubMed](#)]
23. Menke-van der Houven van Oordt, C.W.; Gootjes, E.C.; Huisman, M.C.; Vugts, D.J.; Roth, C.; Luik, A.M.; Mulder, E.R.; Schuit, R.C.; Boellaard, R.; Hoekstra, O.S.; et al. ⁸⁹Zr-cetuximab PET imaging in patients with advanced colorectal cancer. *Oncotarget* **2015**, *6*, 30384–30393. [[CrossRef](#)] [[PubMed](#)]
24. Makris, N.E.; Boellaard, R.; van Lingen, A.; Lammertsma, A.A.; van Dongen, G.A.; Verheul, H.M.; Menke, C.W.; Huisman, M.C. PET/CT-derived whole-body and bone marrow dosimetry of ⁸⁹Zr-cetuximab. *J. Nucl. Med.* **2015**, *56*, 249–254. [[CrossRef](#)] [[PubMed](#)]
25. Jauw, Y.W.; Zijlstra, J.M.; de Jong, D.; Vugts, D.J.; Zweegman, S.; Hoekstra, O.S.; van Dongen, G.A.; Huisman, M.C. Performance of ⁸⁹Zr-Labeled-Rituximab-PET as an Imaging Biomarker to Assess CD20 Targeting: A Pilot Study in Patients with Relapsed/Refractory Diffuse Large B Cell Lymphoma. *PLoS ONE* **2017**, *12*, e0169828. [[CrossRef](#)]
26. Bruijnen, S.; Tsang, A.S.M.; Raterman, H.; Ramwadhoebe, T.; Vugts, D.; van Dongen, G.; Huisman, M.; Hoekstra, O.; Tak, P.P.; Voskuyl, A.; et al. B-cell imaging with zirconium-89 labelled rituximab PET-CT at baseline is associated with therapeutic response 24 weeks after initiation of rituximab treatment in rheumatoid arthritis patients. *Arthritis Res. Ther.* **2016**, *18*, 266. [[CrossRef](#)]
27. Pool, M.; Kol, A.; Lub-de Hooge, M.N.; Gerdes, C.A.; de Jong, S.; de Vries, E.G.; Terwisscha van Scheltinga, A.G. Extracellular domain shedding influences specific tumor uptake and organ distribution of the EGFR PET tracer ⁸⁹Zr-imagatuzumab. *Oncotarget* **2016**, *7*, 68111–68121. [[CrossRef](#)]
28. Meijs, W.E.; Haisma, H.J.; Klok, R.P.; van Gog, F.B.; Kievit, E.; Pinedo, H.M.; Herscheid, J.D. Zirconium-labeled monoclonal antibodies and their distribution in tumor-bearing nude mice. *J. Nucl. Med.* **1997**, *38*, 112–118.

29. Borjesson, P.K.; Jauw, Y.W.; Boellaard, R.; de Bree, R.; Comans, E.F.; Roos, J.C.; Castelijns, J.A.; Vosjan, M.J.; Kummer, J.A.; Leemans, C.R.; et al. Performance of immuno-positron emission tomography with zirconium-89-labeled chimeric monoclonal antibody U36 in the detection of lymph node metastases in head and neck cancer patients. *Clin. Cancer Res.* **2006**, *12*, 2133–2140. [[CrossRef](#)]
30. Abou, D.S.; Ku, T.; Smith-Jones, P.M. In vivo biodistribution and accumulation of ⁸⁹Zr in mice. *Nucl. Med. Biol.* **2011**, *38*, 675–681. [[CrossRef](#)]
31. Gross, M.E.; Shazer, R.L.; Agus, D.B. Targeting the HER-kinase axis in cancer. *Semin. Oncol.* **2004**, *31*, 9–20. [[CrossRef](#)] [[PubMed](#)]
32. Marquez, B.V.; Ikotun, O.F.; Zheleznyak, A.; Wright, B.; Hari-Raj, A.; Pierce, R.A.; Lapi, S.E. Evaluation of (⁸⁹Zr)-pertuzumab in Breast cancer xenografts. *Mol. Pharm.* **2014**, *11*, 3988–3995. [[CrossRef](#)] [[PubMed](#)]
33. Ulaner, G.A.; Lyashchenko, S.K.; Riedl, C.; Ruan, S.; Zanzonico, P.B.; Lake, D.; Jhaveri, K.; Zeglis, B.; Lewis, J.S.; O'Donoghue, J.A. First-in-Human Human Epidermal Growth Factor Receptor 2-Targeted Imaging Using (⁸⁹Zr)-Pertuzumab PET/CT: Dosimetry and Clinical Application in Patients with Breast Cancer. *J. Nucl. Med.* **2018**, *59*, 900–906. [[CrossRef](#)] [[PubMed](#)]
34. Abdel-Nabi, H.; Doerr, R.J.; Chan, H.W.; Balu, D.; Schmelter, R.F.; Maguire, R.T. In-¹¹¹In-labeled monoclonal antibody immunoscintigraphy in colorectal carcinoma: Safety, sensitivity, and preliminary clinical results. *Radiology* **1990**, *175*, 163–171. [[CrossRef](#)]
35. Wong, J.Y.; Raubitschek, A.; Yamauchi, D.; Williams, L.E.; Wu, A.M.; Yazaki, P.; Shively, J.E.; Colcher, D.; Somlo, G. A pretherapy biodistribution and dosimetry study of indium-111-radiolabeled trastuzumab in patients with human epidermal growth factor receptor 2-overexpressing breast cancer. *Cancer Biother. Radiopharm.* **2010**, *25*, 387–394. [[CrossRef](#)]
36. O'Donoghue, J.A.; Lewis, J.S.; Pandit-Taskar, N.; Fleming, S.E.; Schoder, H.; Larson, S.M.; Beylergil, V.; Ruan, S.; Lyashchenko, S.K.; Zanzonico, P.B.; et al. Pharmacokinetics, Biodistribution, and Radiation Dosimetry for (⁸⁹Zr)-Trastuzumab in Patients with Esophagogastric Cancer. *J. Nucl. Med.* **2018**, *59*, 161–166. [[CrossRef](#)]
37. Ulaner, G.A.; Hyman, D.M.; Lyashchenko, S.K.; Lewis, J.S.; Carrasquillo, J.A. ⁸⁹Zr-Trastuzumab PET/CT for Detection of Human Epidermal Growth Factor Receptor 2-Positive Metastases in Patients With Human Epidermal Growth Factor Receptor 2-Negative Primary Breast Cancer. *Clin. Nucl. Med.* **2017**, *42*, 912–917. [[CrossRef](#)]
38. Bensch, F.; Brouwers, A.H.; Lub-de Hooge, M.N.; de Jong, J.R.; van der Vegt, B.; Sleijfer, S.; de Vries, E.G.E.; Schroder, C.P. (⁸⁹Zr)-trastuzumab PET supports clinical decision making in breast cancer patients, when HER2 status cannot be determined by standard work up. *Eur. J. Nucl. Med. Mol. Imaging* **2018**, *45*, 2300–2306. [[CrossRef](#)]
39. Dehdashti, F.; Wu, N.; Bose, R.; Naughton, M.J.; Ma, C.X.; Marquez-Nostra, B.V.; Diebold, P.; Mpoy, C.; Rogers, B.E.; Lapi, S.E.; et al. Evaluation of [(⁸⁹Zr)]trastuzumab-PET/CT in differentiating HER2-positive from HER2-negative breast cancer. *Breast Cancer Res. Treat.* **2018**, *169*, 523–530. [[CrossRef](#)]
40. Zhang, J.; Song, Q.; Cai, L.; Xie, Y.; Chen, Y. The efficacy of (¹⁷⁷Lu)-DOTATATE peptide receptor radionuclide therapy (PRRT) in patients with metastatic neuroendocrine tumours: A systematic review and meta-analysis. *J. Cancer Res. Clin. Oncol.* **2020**, 1–11. [[CrossRef](#)]
41. Holland, J.P.; Caldas-Lopes, E.; Divilov, V.; Longo, V.A.; Taldone, T.; Zatorska, D.; Chiosis, G.; Lewis, J.S. Measuring the pharmacodynamic effects of a novel Hsp90 inhibitor on HER2/neu expression in mice using Zr-DFO-trastuzumab. *PLoS ONE* **2010**, *5*, e8859. [[CrossRef](#)] [[PubMed](#)]
42. Oude Munnink, T.H.; de Vries, E.G.; Vedelaar, S.R.; Timmer-Bosscha, H.; Schroder, C.P.; Brouwers, A.H.; Lub-de Hooge, M.N. Lapatinib and 17AAG reduce ⁸⁹Zr-trastuzumab-F(ab')₂ uptake in SKBR3 tumor xenografts. *Mol. Pharm.* **2012**, *9*, 2995–3002. [[CrossRef](#)] [[PubMed](#)]
43. Sanchez-Vega, F.; Hechtman, J.F.; Castel, P.; Ku, G.Y.; Tuvy, Y.; Won, H.; Fong, C.J.; Bouvier, N.; Nanjangud, G.J.; Soong, J.; et al. EGFR and MET Amplifications Determine Response to HER2 Inhibition in ERBB2-Amplified Esophagogastric Cancer. *Cancer Discov.* **2019**, *9*, 199–209. [[CrossRef](#)]
44. Carmon, K.S.; Azhdarinia, A. Application of Immuno-PET in Antibody-Drug Conjugate Development. *Mol. Imaging* **2018**, *17*, 1536012118801223. [[CrossRef](#)] [[PubMed](#)]

45. Gebhart, G.; Lamberts, L.E.; Wimana, Z.; Garcia, C.; Emonts, P.; Ameye, L.; Stroobants, S.; Huizing, M.; Aftimos, P.; Tol, J.; et al. Molecular imaging as a tool to investigate heterogeneity of advanced HER2-positive breast cancer and to predict patient outcome under trastuzumab emtansine (T-DM1): The ZEPHIR trial. *Ann. Oncol.* **2016**, *27*, 619–624. [[CrossRef](#)]
46. Ciardiello, F.; Tortora, G. Epidermal growth factor receptor (EGFR) as a target in cancer therapy: Understanding the role of receptor expression and other molecular determinants that could influence the response to anti-EGFR drugs. *Eur. J. Cancer* **2003**, *39*, 1348–1354. [[CrossRef](#)]
47. Vallabhajosula, S.; Nikolopoulou, A.; Jhanwar, Y.S.; Kaur, G.; Tagawa, S.T.; Nanus, D.M.; Bander, N.H.; Goldsmith, S.J. Radioimmunotherapy of Metastatic Prostate Cancer with (1)(7)(7)Lu-DOTAhuJ591 Anti Prostate Specific Membrane Antigen Specific Monoclonal Antibody. *Curr. Radiopharm.* **2016**, *9*, 44–53. [[CrossRef](#)]
48. Perk, L.R.; Visser, G.W.; Vosjan, M.J.; Stigter-van Walsum, M.; Tjink, B.M.; Leemans, C.R.; van Dongen, G.A. (89)Zr as a PET surrogate radioisotope for scouting biodistribution of the therapeutic radiometals (90)Y and (177)Lu in tumor-bearing nude mice after coupling to the internalizing antibody cetuximab. *J. Nucl. Med.* **2005**, *46*, 1898–1906.
49. Chekol, R.; Solomon, V.R.; Alizadeh, E.; Bernhard, W.; Fisher, D.; Hill, W.; Barreto, K.; DeCoteau, J.F.; Parada, A.C.; Geyer, C.R.; et al. (89)Zr-nimotuzumab for immunoPET imaging of epidermal growth factor receptor I. *Oncotarget* **2018**, *9*, 17117–17132. [[CrossRef](#)]
50. Nayak, T.K.; Garmestani, K.; Milenic, D.E.; Brechbiel, M.W. PET and MRI of metastatic peritoneal and pulmonary colorectal cancer in mice with human epidermal growth factor receptor 1-targeted 89Zr-labeled panitumumab. *J. Nucl. Med.* **2012**, *53*, 113–120. [[CrossRef](#)] [[PubMed](#)]
51. Lindenberg, L.; Adler, S.; Turkbey, I.B.; Mertan, F.; Ton, A.; Do, K.; Kummar, S.; Gonzalez, E.M.; Bhattacharyya, S.; Jacobs, P.M.; et al. Dosimetry and first human experience with (89)Zr-panitumumab. *Am. J. Nucl. Med. Mol. Imaging* **2017**, *7*, 195–203. [[PubMed](#)]
52. Burley, T.A.; Da Pieve, C.; Martins, C.D.; Ciobota, D.M.; Allott, L.; Oyen, W.J.G.; Harrington, K.J.; Smith, G.; Kramer-Marek, G. Affibody-Based PET Imaging to Guide EGFR-Targeted Cancer Therapy in Head and Neck Squamous Cell Cancer Models. *J. Nucl. Med.* **2019**, *60*, 353–361. [[CrossRef](#)] [[PubMed](#)]
53. Peach, C.J.; Mignone, V.W.; Arruda, M.A.; Alcobia, D.C.; Hill, S.J.; Kilpatrick, L.E.; Woolard, J. Molecular Pharmacology of VEGF-A Isoforms: Binding and Signalling at VEGFR2. *Int. J. Mol. Sci.* **2018**, *19*, 1264. [[CrossRef](#)]
54. Jansen, M.H.; Veldhuijzen van Zanten, S.E.M.; van Vuurden, D.G.; Huisman, M.C.; Vugts, D.J.; Hoekstra, O.S.; van Dongen, G.A.; Kaspers, G.L. Molecular Drug Imaging: (89)Zr-Bevacizumab PET in Children with Diffuse Intrinsic Pontine Glioma. *J. Nucl. Med.* **2017**, *58*, 711–716. [[CrossRef](#)]
55. Van der Bilt, A.R.; Terwisscha van Scheltinga, A.G.; Timmer-Bosscha, H.; Schroder, C.P.; Pot, L.; Kosterink, J.G.; van der Zee, A.G.; Lub-de Hooge, M.N.; de Jong, S.; de Vries, E.G.; et al. Measurement of tumor VEGF-A levels with 89Zr-bevacizumab PET as an early biomarker for the antiangiogenic effect of everolimus treatment in an ovarian cancer xenograft model. *Clin. Cancer Res.* **2012**, *18*, 6306–6314. [[CrossRef](#)] [[PubMed](#)]
56. Van Es, S.C.; Brouwers, A.H.; Mahesh, S.V.K.; Leliveld-Kors, A.M.; de Jong, I.J.; Lub-de Hooge, M.N.; de Vries, E.G.E.; Gietema, J.A.; Oosting, S.F. (89)Zr-Bevacizumab PET: Potential Early Indicator of Everolimus Efficacy in Patients with Metastatic Renal Cell Carcinoma. *J. Nucl. Med.* **2017**, *58*, 905–910. [[CrossRef](#)]
57. Le Tourneau, C.; Raymond, E.; Faivre, S. Sunitinib: A novel tyrosine kinase inhibitor. A brief review of its therapeutic potential in the treatment of renal carcinoma and gastrointestinal stromal tumors (GIST). *Ther. Clin. Risk Manag.* **2007**, *3*, 341–348. [[CrossRef](#)]
58. Nagengast, W.B.; Lub-de Hooge, M.N.; Oosting, S.F.; den Dunnen, W.F.; Warnders, F.J.; Brouwers, A.H.; de Jong, J.R.; Price, P.M.; Hollema, H.; Hospers, G.A.; et al. VEGF-PET imaging is a noninvasive biomarker showing differential changes in the tumor during sunitinib treatment. *Cancer Res.* **2011**, *71*, 143–153. [[CrossRef](#)]
59. Van Meerten, T.; Hagenbeek, A. CD20-targeted therapy: The next generation of antibodies. *Semin. Hematol.* **2010**, *47*, 199–210. [[CrossRef](#)]
60. Hanaoka, K.; Hosono, M.; Tatsumi, Y.; Ishii, K.; Im, S.W.; Tsuchiya, N.; Sakaguchi, K.; Matsumura, I. Heterogeneity of intratumoral (111)In-ibratumomab tiuxetan and (18)F-FDG distribution in association with therapeutic response in radioimmunotherapy for B-cell non-Hodgkin's lymphoma. *EJNMMI Res.* **2015**, *5*, 10. [[CrossRef](#)] [[PubMed](#)]

61. Perk, L.R.; Visser, O.J.; Stigter-van Walsum, M.; Vosjan, M.J.; Visser, G.W.; Zijlstra, J.M.; Huijgens, P.C.; van Dongen, G.A. Preparation and evaluation of (89)Zr-Zevalin for monitoring of (90)Y-Zevalin biodistribution with positron emission tomography. *Eur. J. Nucl. Med. Mol. Imaging* **2006**, *33*, 1337–1345. [[CrossRef](#)] [[PubMed](#)]
62. Rizvi, S.N.; Visser, O.J.; Vosjan, M.J.; van Lingen, A.; Hoekstra, O.S.; Zijlstra, J.M.; Huijgens, P.C.; van Dongen, G.A.; Lubberink, M. Biodistribution, radiation dosimetry and scouting of 90Y-ibritumomab tiuxetan therapy in patients with relapsed B-cell non-Hodgkin's lymphoma using 89Zr-ibritumomab tiuxetan and PET. *Eur. J. Nucl. Med. Mol. Imaging* **2012**, *39*, 512–520. [[CrossRef](#)] [[PubMed](#)]
63. De Jong, A.; Mous, R.; van Dongen, G.A.; Hoekstra, O.S.; Nievelstein, R.A.; de Keizer, B. (89) Zr-rituximab PET/CT to detect neurolymphomatosis. *Am. J. Hematol.* **2016**, *91*, 649–650. [[CrossRef](#)] [[PubMed](#)]
64. Dorner, T.; Burmester, G.R. The role of B cells in rheumatoid arthritis: Mechanisms and therapeutic targets. *Curr. Opin Rheumatol.* **2003**, *15*, 246–252. [[CrossRef](#)]
65. Rahbar, K.; Afshar-Oromieh, A.; Jadvar, H.; Ahmadzadehfar, H. PSMA Theranostics: Current Status and Future Directions. *Mol. Imaging* **2018**, *17*, 1536012118776068. [[CrossRef](#)]
66. Ruggiero, A.; Holland, J.P.; Hudolin, T.; Shenker, L.; Koulova, A.; Bander, N.H.; Lewis, J.S.; Grimm, J. Targeting the internal epitope of prostate-specific membrane antigen with 89Zr-7E11 immuno-PET. *J. Nucl. Med.* **2011**, *52*, 1608–1615. [[CrossRef](#)]
67. Osborne, J.R.; Green, D.A.; Spratt, D.E.; Lyashchenko, S.; Fareedy, S.B.; Robinson, B.D.; Beattie, B.J.; Jain, M.; Lewis, J.S.; Christos, P.; et al. A prospective pilot study of (89)Zr-J591/prostate specific membrane antigen positron emission tomography in men with localized prostate cancer undergoing radical prostatectomy. *J. Urol.* **2014**, *191*, 1439–1445. [[CrossRef](#)]
68. Pandit-Taskar, N.; O'Donoghue, J.A.; Beylgeril, V.; Lyashchenko, S.; Ruan, S.; Solomon, S.B.; Durack, J.C.; Carrasquillo, J.A.; Lefkowitz, R.A.; Gonen, M.; et al. (8)(9)Zr-huJ591 immuno-PET imaging in patients with advanced metastatic prostate cancer. *Eur. J. Nucl. Med. Mol. Imaging* **2014**, *41*, 2093–2105. [[CrossRef](#)]
69. Pandit-Taskar, N.; O'Donoghue, J.A.; Durack, J.C.; Lyashchenko, S.K.; Cheal, S.M.; Beylgeril, V.; Lefkowitz, R.A.; Carrasquillo, J.A.; Martinez, D.F.; Fung, A.M.; et al. A Phase I/II Study for Analytic Validation of 89Zr-J591 ImmunoPET as a Molecular Imaging Agent for Metastatic Prostate Cancer. *Clin. Cancer Res.* **2015**, *21*, 5277–5285. [[CrossRef](#)]
70. Cornelis, F.H.; Durack, J.C.; Pandit-Taskar, N.; Ulaner, G.A.; Lewis, J.S.; Morris, M.J.; Solomon, S.B. Long-Half-Life (89)Zr-Labeled Radiotracers Can Guide Percutaneous Biopsy Within the PET/CT Suite Without ReInjection of Radiotracer. *J. Nucl. Med.* **2018**, *59*, 399–402. [[CrossRef](#)]
71. Viola-Villegas, N.T.; Sevak, K.K.; Carlin, S.D.; Doran, M.G.; Evans, H.W.; Bartlett, D.W.; Wu, A.M.; Lewis, J.S. Noninvasive Imaging of PSMA in prostate tumors with (89)Zr-Labeled huJ591 engineered antibody fragments: The faster alternatives. *Mol. Pharm.* **2014**, *11*, 3965–3973. [[CrossRef](#)] [[PubMed](#)]
72. Joraku, A.; Hatano, K.; Kawai, K.; Kandori, S.; Kojima, T.; Fukumitsu, N.; Isobe, T.; Mori, Y.; Sakata, M.; Hara, T.; et al. Phase I/IIa PET imaging study with (89)zirconium labeled anti-PSMA minibody for urological malignancies. *Ann. Nucl. Med.* **2019**, *33*, 119–127. [[CrossRef](#)] [[PubMed](#)]
73. Matsuda, M.; Ishikawa, E.; Yamamoto, T.; Hatano, K.; Joraku, A.; Iizumi, Y.; Masuda, Y.; Nishiyama, H.; Matsumura, A. Potential use of prostate specific membrane antigen (PSMA) for detecting the tumor neovasculature of brain tumors by PET imaging with (89)Zr-Df-IAB2M anti-PSMA minibody. *J. Neurooncol.* **2018**, *138*, 581–589. [[CrossRef](#)] [[PubMed](#)]
74. Pandit-Taskar, N.; O'Donoghue, J.A.; Ruan, S.; Lyashchenko, S.K.; Carrasquillo, J.A.; Heller, G.; Martinez, D.F.; Cheal, S.M.; Lewis, J.S.; Fleisher, M.; et al. First-in-Human Imaging with 89Zr-Df-IAB2M Anti-PSMA Minibody in Patients with Metastatic Prostate Cancer: Pharmacokinetics, Biodistribution, Dosimetry, and Lesion Uptake. *J. Nucl. Med.* **2016**, *57*, 1858–1864. [[CrossRef](#)]
75. Mishra, M.N.; Chandavarkar, V.; Sharma, R.; Bhargava, D. Structure, function and role of CD44 in neoplasia. *J. Oral. Maxillofac. Pathol.* **2019**, *23*, 267–272. [[CrossRef](#)]
76. Verel, I.; Visser, G.W.; Boellaard, R.; Boerman, O.C.; van Eerd, J.; Snow, G.B.; Lammertsma, A.A.; van Dongen, G.A. Quantitative 89Zr immuno-PET for in vivo scouting of 90Y-labeled monoclonal antibodies in xenograft-bearing nude mice. *J. Nucl. Med.* **2003**, *44*, 1663–1670.
77. Vugts, D.J.; Heuveling, D.A.; Stigter-van Walsum, M.; Weigand, S.; Bergstrom, M.; van Dongen, G.A.; Nayak, T.K. Preclinical evaluation of 89Zr-labeled anti-CD44 monoclonal antibody RG7356 in mice and cynomolgus monkeys: Prelude to Phase 1 clinical studies. *MAbs* **2014**, *6*, 567–575. [[CrossRef](#)]

78. Gala, K.; Chandarlapaty, S. Molecular pathways: HER3 targeted therapy. *Clin. Cancer Res.* **2014**, *20*, 1410–1416. [[CrossRef](#)]
79. Bensch, F.; Lamberts, L.E.; Smeenk, M.M.; Jorritsma-Smit, A.; Lub-de Hooge, M.N.; Terwisscha van Scheltinga, A.G.T.; de Jong, J.R.; Gietema, J.A.; Schroder, C.P.; Thomas, M.; et al. (89)Zr-Lumretuzumab PET Imaging before and during HER3 Antibody Lumretuzumab Treatment in Patients with Solid Tumors. *Clin. Cancer Res.* **2017**, *23*, 6128–6137. [[CrossRef](#)]
80. Menke-van der Houven van Oordt, C.W.; McGeoch, A.; Bergstrom, M.; McSherry, I.; Smith, D.A.; Cleveland, M.; Al-Azzam, W.; Chen, L.; Verheul, H.; Hoekstra, O.S.; et al. Immuno-PET Imaging to Assess Target Engagement: Experience from (89)Zr-Anti-HER3 mAb (GSK2849330) in Patients with Solid Tumors. *J. Nucl. Med.* **2019**, *60*, 902–909. [[CrossRef](#)]
81. Martins, C.D.; Da Pieve, C.; Burley, T.A.; Smith, R.; Ciobota, D.M.; Allott, L.; Harrington, K.J.; Oyen, W.J.G.; Smith, G.; Kramer-Marek, G. HER3-Mediated Resistance to Hsp90 Inhibition Detected in Breast Cancer Xenografts by Affibody-Based PET Imaging. *Clin. Cancer Res.* **2018**, *24*, 1853–1865. [[CrossRef](#)] [[PubMed](#)]
82. Esfahani, K.; Roudaia, L.; Buhlaiga, N.; Del Rincon, S.V.; Papneja, N.; Miller, W.H., Jr. A review of cancer immunotherapy: From the past, to the present, to the future. *Curr. Oncol.* **2020**, *27*, S87–S97. [[CrossRef](#)] [[PubMed](#)]
83. England, C.G.; Jiang, D.; Ehlerding, E.B.; Rekoske, B.T.; Ellison, P.A.; Hernandez, R.; Barnhart, T.E.; McNeel, D.G.; Huang, P.; Cai, W. (89)Zr-labeled nivolumab for imaging of T-cell infiltration in a humanized murine model of lung cancer. *Eur. J. Nucl. Med. Mol. Imaging* **2018**, *45*, 110–120. [[CrossRef](#)]
84. Bensch, F.; van der Veen, E.L.; Lub-de Hooge, M.N.; Jorritsma-Smit, A.; Boellaard, R.; Kok, I.C.; Oosting, S.F.; Schroder, C.P.; Hiltermann, T.J.N.; van der Wekken, A.J.; et al. (89)Zr-atezolizumab imaging as a non-invasive approach to assess clinical response to PD-L1 blockade in cancer. *Nat. Med.* **2018**, *24*, 1852–1858. [[CrossRef](#)] [[PubMed](#)]
85. Radvanyi, L.G. Tumor-Infiltrating Lymphocyte Therapy: Addressing Prevailing Questions. *Cancer J.* **2015**, *21*, 450–464. [[CrossRef](#)] [[PubMed](#)]
86. Beckford Vera, D.R.; Smith, C.C.; Bixby, L.M.; Glatt, D.M.; Dunn, S.S.; Saito, R.; Kim, W.Y.; Serody, J.S.; Vincent, B.G.; Parrott, M.C. Immuno-PET imaging of tumor-infiltrating lymphocytes using zirconium-89 radiolabeled anti-CD3 antibody in immune-competent mice bearing syngeneic tumors. *PLoS ONE* **2018**, *13*, e0193832. [[CrossRef](#)]
87. Larimer, B.M.; Wehrenberg-Klee, E.; Caraballo, A.; Mahmood, U. Quantitative CD3 PET Imaging Predicts Tumor Growth Response to Anti-CTLA-4 Therapy. *J. Nucl. Med.* **2016**, *57*, 1607–1611. [[CrossRef](#)]
88. Tavare, R.; McCracken, M.N.; Zettlitz, K.A.; Salazar, F.B.; Olafsen, T.; Witte, O.N.; Wu, A.M. Immuno-PET of Murine T Cell Reconstitution Postadoptive Stem Cell Transplantation Using Anti-CD4 and Anti-CD8 Cys-Diabodies. *J. Nucl. Med.* **2015**, *56*, 1258–1264. [[CrossRef](#)]
89. Waaijer, S.J.; Giesen, D.; Ishiguro, T.; Sano, Y.; Sugaya, N.; Schroder, C.P.; de Vries, E.G.; Lub-de Hooge, M.N. Preclinical PET imaging of bispecific antibody ERY974 targeting CD3 and glypican 3 reveals that tumor uptake correlates to T cell infiltrate. *J. Immunother. Cancer* **2020**, *8*. [[CrossRef](#)]
90. Farzin, L.; Sheibani, S.; Moassesi, M.E.; Shamsipur, M. An overview of nanoscale radionuclides and radiolabeled nanomaterials commonly used for nuclear molecular imaging and therapeutic functions. *J. Biomed. Mater. Res. A* **2019**, *107*, 251–285. [[CrossRef](#)]
91. Perez-Medina, C.; Tang, J.; Abdel-Atti, D.; Hogstad, B.; Merad, M.; Fisher, E.A.; Fayad, Z.A.; Lewis, J.S.; Mulder, W.J.; Reiner, T. PET Imaging of Tumor-Associated Macrophages with 89Zr-Labeled High-Density Lipoprotein Nanoparticles. *J. Nucl. Med.* **2015**, *56*, 1272–1277. [[CrossRef](#)] [[PubMed](#)]
92. Keliher, E.J.; Yoo, J.; Nahrendorf, M.; Lewis, J.S.; Marinelli, B.; Newton, A.; Pittet, M.J.; Weissleder, R. 89Zr-labeled dextran nanoparticles allow in vivo macrophage imaging. *Bioconjug. Chem.* **2011**, *22*, 2383–2389. [[CrossRef](#)] [[PubMed](#)]
93. Heuveling, D.A.; Visser, G.W.; Baclayon, M.; Roos, W.H.; Wuite, G.J.; Hoekstra, O.S.; Leemans, C.R.; de Bree, R.; van Dongen, G.A. 89Zr-nanocolloidal albumin-based PET/CT lymphoscintigraphy for sentinel node detection in head and neck cancer: Preclinical results. *J. Nucl. Med.* **2011**, *52*, 1580–1584. [[CrossRef](#)]
94. Heuveling, D.A.; van Schie, A.; Vugts, D.J.; Hendrikse, N.H.; Yaqub, M.; Hoekstra, O.S.; Karagozoglu, K.H.; Leemans, C.R.; van Dongen, G.A.; de Bree, R. Pilot study on the feasibility of PET/CT lymphoscintigraphy with 89Zr-nanocolloidal albumin for sentinel node identification in oral cancer patients. *J. Nucl. Med.* **2013**, *54*, 585–589. [[CrossRef](#)] [[PubMed](#)]

95. Heuveling, D.A.; Karagozoglou, K.H.; Van Lingen, A.; Hoekstra, O.S.; Van Dongen, G.; De Bree, R. Feasibility of intraoperative detection of sentinel lymph nodes with 89-zirconium-labelled nanocolloidal albumin PET-CT and a handheld high-energy gamma probe. *EJNMMI Res.* **2018**, *8*, 15. [[CrossRef](#)]
96. Ankersmit, M.; Hoekstra, O.S.; van Lingen, A.; Bloemena, E.; Jacobs, M.; Vugts, D.J.; Bonjer, H.J.; van Dongen, G.; Meijerink, W. Perioperative PET/CT lymphoscintigraphy and fluorescent real-time imaging for sentinel lymph node mapping in early staged colon cancer. *Eur. J. Nucl. Med. Mol. Imaging* **2019**, *46*, 1495–1505. [[CrossRef](#)]
97. Zheng, K.H.; van der Valk, F.M.; Smits, L.P.; Sandberg, M.; Dasseux, J.L.; Baron, R.; Barbaras, R.; Keyserling, C.; Coolen, B.F.; Nederveen, A.J.; et al. HDL mimetic CER-001 targets atherosclerotic plaques in patients. *Atherosclerosis* **2016**, *251*, 381–388. [[CrossRef](#)]
98. Perez-Medina, C.; Binderup, T.; Lobatto, M.E.; Tang, J.; Calcagno, C.; Giesen, L.; Wessel, C.H.; Witjes, J.; Ishino, S.; Baxter, S.; et al. In Vivo PET Imaging of HDL in Multiple Atherosclerosis Models. *JACC Cardiovasc. Imaging* **2016**, *9*, 950–961. [[CrossRef](#)]
99. Beldman, T.J.; Senders, M.L.; Alaarg, A.; Perez-Medina, C.; Tang, J.; Zhao, Y.; Fay, F.; Deichmoller, J.; Born, B.; Desclos, E.; et al. Hyaluronan Nanoparticles Selectively Target Plaque-Associated Macrophages and Improve Plaque Stability in Atherosclerosis. *ACS Nano* **2017**, *11*, 5785–5799. [[CrossRef](#)]
100. Majmudar, M.D.; Yoo, J.; Keliher, E.J.; Truelove, J.J.; Iwamoto, Y.; Sena, B.; Dutta, P.; Borodovsky, A.; Fitzgerald, K.; Di Carli, M.F.; et al. Polymeric nanoparticle PET/MR imaging allows macrophage detection in atherosclerotic plaques. *Circ. Res.* **2013**, *112*, 755–761. [[CrossRef](#)]
101. Ruggiero, A.; Holland, J.P.; Lewis, J.S.; Grimm, J. Cerenkov luminescence imaging of medical isotopes. *J. Nucl. Med.* **2010**, *51*, 1123–1130. [[CrossRef](#)] [[PubMed](#)]
102. Kamkaew, A.; Chen, F.; Zhan, Y.; Majewski, R.L.; Cai, W. Scintillating Nanoparticles as Energy Mediators for Enhanced Photodynamic Therapy. *ACS Nano* **2016**, *10*, 3918–3935. [[CrossRef](#)]
103. Welling, M.M.; Duijvestein, M.; Signore, A.; van der Weerd, L. In vivo biodistribution of stem cells using molecular nuclear medicine imaging. *J. Cell Physiol.* **2011**, *226*, 1444–1452. [[CrossRef](#)]
104. Zhao, Z.; Chen, Y.; Francisco, N.M.; Zhang, Y.; Wu, M. The application of CAR-T cell therapy in hematological malignancies: Advantages and challenges. *Acta Pharm. Sin. B* **2018**, *8*, 539–551. [[CrossRef](#)] [[PubMed](#)]
105. Weist, M.R.; Starr, R.; Aguilar, B.; Chea, J.; Miles, J.K.; Poku, E.; Gerds, E.; Yang, X.; Priceman, S.J.; Forman, S.J.; et al. PET of Adoptively Transferred Chimeric Antigen Receptor T Cells with (89)Zr-Oxine. *J. Nucl. Med.* **2018**, *59*, 1531–1537. [[CrossRef](#)] [[PubMed](#)]
106. Yusufi, N.; Mall, S.; Bianchi, H.O.; Steiger, K.; Reder, S.; Klar, R.; Audehm, S.; Mustafa, M.; Nekolla, S.; Peschel, C.; et al. In-depth Characterization of a TCR-specific Tracer for Sensitive Detection of Tumor-directed Transgenic T Cells by Immuno-PET. *Theranostics* **2017**, *7*, 2402–2416. [[CrossRef](#)] [[PubMed](#)]
107. Bansal, A.; Pandey, M.K.; Demirhan, Y.E.; Nesbitt, J.J.; Crespo-Diaz, R.J.; Terzic, A.; Behfar, A.; DeGrado, T.R. Novel (89)Zr cell labeling approach for PET-based cell trafficking studies. *EJNMMI Res.* **2015**, *5*, 19. [[CrossRef](#)] [[PubMed](#)]
108. Yang, B.; Brahmabhatt, A.; Nieves Torres, E.; Thielen, B.; McCall, D.L.; Engel, S.; Bansal, A.; Pandey, M.K.; Dietz, A.B.; Leof, E.B.; et al. Tracking and Therapeutic Value of Human Adipose Tissue-derived Mesenchymal Stem Cell Transplantation in Reducing Venous Neointimal Hyperplasia Associated with Arteriovenous Fistula. *Radiology* **2016**, *279*, 513–522. [[CrossRef](#)]
109. Nicolas, C.T.; Hickey, R.D.; Allen, K.L.; Du, Z.; Guthman, R.M.; Kaiser, R.A.; Amiot, B.; Bansal, A.; Pandey, M.K.; Suksanpaisan, L.; et al. Hepatocyte spheroids as an alternative to single cells for transplantation after ex vivo gene therapy in mice and pig models. *Surgery* **2018**, *164*, 473–481. [[CrossRef](#)]
110. Ellison, P.A.; Valdovinos, H.F.; Graves, S.A.; Barnhart, T.E.; Nickles, R.J. Spot-welding solid targets for high current cyclotron irradiation. *Appl. Radiat. Isot.* **2016**, *118*, 350–353. [[CrossRef](#)]
111. Siikanen, J.; Tran, T.A.; Olsson, T.G.; Strand, S.E.; Sandell, A. A solid target system with remote handling of irradiated targets for PET cyclotrons. *Appl. Radiat. Isot.* **2014**, *94*, 294–301. [[CrossRef](#)] [[PubMed](#)]
112. Dias, G.M.; Ramogida, C.F.; Rousseau, J.; Zacchia, N.A.; Hoehr, C.; Schaffer, P.; Lin, K.S.; Benard, F. (89)Zr for antibody labeling and in vivo studies—A comparison between liquid and solid target production. *Nucl. Med. Biol.* **2018**, *58*, 1–7. [[CrossRef](#)]
113. Pandey, M.K.; Bansal, A.; Engelbrecht, H.P.; Byrne, J.F.; Packard, A.B.; DeGrado, T.R. Improved production and processing of (8)(9)Zr using a solution target. *Nucl. Med. Biol.* **2016**, *43*, 97–100. [[CrossRef](#)] [[PubMed](#)]

114. Zhai, C.; He, S.; Ye, Y.; Rangger, C.; Kaeopookum, P.; Summer, D.; Haas, H.; Kremser, L.; Lindner, H.; Foster, J.; et al. Rational Design, Synthesis and Preliminary Evaluation of Novel Fusarinine C-Based Chelators for Radiolabeling with Zirconium-89. *Biomolecules* **2019**, *9*, 91. [[CrossRef](#)] [[PubMed](#)]
115. Adumeau, P.; Davydova, M.; Zeglis, B.M. Thiol-Reactive Bifunctional Chelators for the Creation of Site-Selectively Modified Radioimmunoconjugates with Improved Stability. *Bioconjug. Chem.* **2018**, *29*, 1364–1372. [[CrossRef](#)]
116. Seibold, U.; Wangler, B.; Wangler, C. Rational Design, Development, and Stability Assessment of a Macrocyclic Four-Hydroxamate-Bearing Bifunctional Chelating Agent for (89) Zr. *ChemMedChem* **2017**, *12*, 1555–1571. [[CrossRef](#)]
117. Rousseau, J.; Zhang, Z.; Dias, G.M.; Zhang, C.; Colpo, N.; Benard, F.; Lin, K.S. Design, synthesis and evaluation of novel bifunctional tetrahydroxamate chelators for PET imaging of (89)Zr-labeled antibodies. *Bioorg Med. Chem. Lett.* **2017**, *27*, 708–712. [[CrossRef](#)]
118. Petrik, M.; Zhai, C.; Haas, H.; Decristoforo, C. Siderophores for molecular imaging applications. *Clin. Transl. Imaging* **2017**, *5*, 15–27. [[CrossRef](#)]
119. Buchwalder, C.; Rodriguez-Rodriguez, C.; Schaffer, P.; Karagiozov, S.K.; Saatchi, K.; Hafeli, U.O. A new tetrapodal 3-hydroxy-4-pyridinone ligand for complexation of (89)zirconium for positron emission tomography (PET) imaging. *Dalton Trans.* **2017**, *46*, 9654–9663. [[CrossRef](#)]
120. Adams, C.J.; Wilson, J.J.; Boros, E. Multifunctional Desferrichrome Analogues as Versatile (89)Zr(IV) Chelators for ImmunoPET Probe Development. *Mol. Pharm.* **2017**, *14*, 2831–2842. [[CrossRef](#)]
121. Schillaci, O.; Urbano, N. Digital PET/CT: A new intriguing chance for clinical nuclear medicine and personalized molecular imaging. *Eur. J. Nucl. Med. Mol. Imaging* **2019**, *46*, 1222–1225. [[CrossRef](#)] [[PubMed](#)]



© 2020 by the authors. Licensee MDPI, Basel, Switzerland. This article is an open access article distributed under the terms and conditions of the Creative Commons Attribution (CC BY) license (<http://creativecommons.org/licenses/by/4.0/>).